Characterization and Optical Gas Sensing Properties of BaSnO3 Synthesized By Novel Technique: Flame Spray Pyrolysis

Merve ZEYREK ONGUN (merve.zeyrek@deu.edu.tr)
Dokuz Eylul Universitesi https://orcid.org/0000-0002-2874-8024
Sibel OGUZLAR
Dokuz Eylul University: Dokuz Eylul Universitesi
Alper S. Akalin
Dokuz Eylul University: Dokuz Eylul Universitesi
Serdar Yildirim
Dokuz Eylul University: Dokuz Eylul Universitesi

Original Research

Keywords: Barium stannate, flame spray pyrolysis, optical gas sensing, EtOH, NH3, acetone

Posted Date: February 17th, 2021

DOI: https://doi.org/10.21203/rs.3.rs-203655/v1

Abstract

Barium stannate ($BaSnO_3$) particles were synthesized using a one-step flame spray pyrolysis (FSP) method. The fabricated ceramic powders were investigated in terms of the structural, morphological, and optical properties by using X-ray diffraction (XRD), Fourier-transform infrared spectroscopy (FTIR), X-Ray photoelectron spectroscopy (XPS), scanning electron microscopy (SEM), zeta particle size analyzer, UV-visible spectroscopy (UV-vis) and photoluminescence spectroscopy (PL). The XRD results showed the structure of $BaSnO_3$ crystals have been obtained when the powders were exposed at high temperature, specifically at 1200 °C. The synthesized particles in the submicron size in a range of 70-980 nm were produced. The optical band gap value of the synthesized crystals was calculated by means of reflectance spectra with the Kubelka-Munk method and found as 3.14 eV. When the powders excited at 375 nm, they exhibited emission bands in the visible and near-infrared region (NIR) of the electromagnetic spectrum. As far as we know, this is the first time $BaSnO_3$ crystals have been synthesized using the FSP technique. In this study, the intensity- and decay time- based gas sensing properties of $BaSnO_3$ embedded in ethyl cellulose thin films when exposed to the vapors of ethanol, acetone, and ammonia were also measured.

1. Introduction

The chemical formula of perovskite oxides is $A^{+2}\ B^{+4}\ X_3^{-2}$, where 'A' and 'B' are two metal ions of various sizes, and X is an anion, which bonds to both cations. Alkaline or rare earth elements are occupied at the position of the corners (A), transition metals (3d, 4d, and 5d) are placed on the central site (B), and oxygen element is located at surface centers (X). Sometimes, as a result of the distortions, the perovskite structures that have a cubic crystalline phase can modify to orthorhombic or tetragonal phase [1]. However, the difference in the symmetries is based on a mismatch of alkaline cations because of the smaller ionic radius to the cubic-octahedral cavity in the octahedral lattice. However, the difference in the symmetries is based on a mismatch of alkaline cations because of the smaller ionic radius to the cubic-octahedral cavity in the octahedral lattice.

The barium stannate ($BaSnO_3$) crystals formed as a cubic perovskite-type belong to the group of alkaline earth stannates ($MSnO_3$, where M = Ba, Sr, Ca, Pb) and n-type semiconductors [2]. $BaSnO_3$ has a wide bandgap value of 3.4 eV [3] and has many applications in the field of optoelectronic devices [4], gas sensors [5], photocatalytic studies [6]. $BaSnO_3$ crystals are used as a gas sensor, which is sensitive to a variety of gases such as O_2 [7], CO_2 [8], CO [9], SO_2 [10], CH_4 [11], and humidity [12]. Cerdà and co-workers have investigated the electrical characteristics of $BaSnO_3$ produced using a wet chemical route method as a function of both the temperature and the gas concentration [13]. It is also used to prepare electrical conductor materials because of its dielectric features [14]. Bévillon et al. defined that barium stannate ceramics as a protonic conductor, because of including trivalent metals and the diffusion of protons once H_2O dissociates in the oxygen vacancies [15]. $BaSnO_3$ crystals have been used in photocatalytic degradation applications. The synthesized $BaSnO_3$ particles are used as a suitable material for

photocatalytic applications such as removal of Eriochrome Black T under the lightning of UV radiation by Moshtaghi and co-workers [16].

Synthesis of pure mixed metal oxide powders such as $BaSnO_3$ is quite difficult. A common synthesis method is to mix barium and tin ions at the molecular level in a position closely together at high temperature. There are many different techniques applied for the synthesis of barium stannate such as sol-gel [17], hydrothermal [18], modified combustion technique [19], the solid-state ceramic method [20] and, wet chemical synthesis method [21], and one-step flame spray pyrolysis (FSP) technique. For the synthesizing of nanoparticles, the FSP is the most favored technique because of reducing the synthesis time and the increased reaction rate. The technique has many advantages such as the control simplicity over the process and the reproducibility of the technique, the ease of the spray of the precursor into the flame with using the high-velocity spray jet, the dispersion potential of the prepared precursor directly in the fuel, and the faster aerosol formation. For this reason, the FSP has been applied many times in the production of nanoscale metal oxides and complex metal oxides. Due to the high-temperature environment of the flame (up to 2500°C, depending on raw materials and flame conditions), product nanoparticles are typically fully oxidized and crystalline. Thus, post-synthesis heat treatment steps are typically not required and the nanopowders can directly be used for further processing. However, in the production of complex metal oxides, a heat treatment process may sometimes be required.

In this report, for the first time, the pure perovskite-type $BaSnO_3$ particles have been synthesized utilizing the FSP method and interpreted in terms of structural, morphological, and optical properties. When the sensing particles excited at 375 nm, they exhibited emission bands in the visible area, and also, a strong peak centered at 944 nm in the near-infrared region (NIR). However, in this study, the optical gas sensing properties of the $BaSnO_3$ nanoparticles embedded in thin films to vapors of ethanol, acetone, and ammonia were presented.

2. Experimental Studies

2.1 Materials and equipment

All chemicals and solvents were used without any further purification. Barium acetate ($Ba(CH_3COO)_2$) and Tin (IV) chloride pentahydrate ($SnCl_4{\times}5H_2O$) were purchased from Sigma-Aldrich. Ethylene glycol and citric acid were also provided from Sigma-Aldrich. Determination of phase structure of produced BSO powders was carried out by Thermo Scientific ARL X-ray diffractometer (XRD) which operates with 45 kV voltage and 44 mA current settings and uses Cu-Kα radiation (1.5405Å). X-ray photoelectron spectroscopy (XPS, Thermo Scientific K-Alpha) with a monochromatic Al-Kα (1486.7 eV) X-ray source and a beam size of 400 nm diameter was carried out to determine elemental composition and surface chemistry for all samples. Microstructure images of particles were captured at different magnifications by using a scanning electron microscope (SEM, Zeiss Sigma 300 VP) with 20 kV accelerating voltage. Particle size analysis of all of the synthesized composites was examined by using a Malvern Zeta Sizer

ZS90. The reflectance spectra of the samples were measured using Thermo Scientific Evolution 600 spectrophotometer. The steady-state photoluminescence (PL) emission/excitation measurements were studied by using a red-sensitive photomultiplier tube equipped spectrofluorometer system (Edinburgh Instruments (UK). The instrument was also equipped with a standard 15 W xenon lamp for steady-state measurements.

2.2 Flame spray pyrolysis process

The general processing of the flame spray pyrolysis system was demonstrated in Fig. 1. In the flame spray pyrolysis technique, a transparent metal ion solution is sprayed as a thin haze into the center of flame which is fuel/oxygen ratio of ½ methane (1.5 L/min)/oxygen (3.0 L/min). Through a syringe pump with a feed rate of 5 mL/min. Then, tiny droplets were created while the solution burns within the flame. The transformation of the salt into the metal-oxide structure occurred upon the pyrolysis reaction. After that, metal oxide atoms aggregate into nanoscale particles and these were collected on a cellulosic filter by using a vacuum pump.

2.3 Synthesis of $BaSnO_3$

In this study, $BaSnO_3$ (BSO) was synthesized by flame spray pyrolysis (FSP). $Ba(CH_3COO)_2$ and $SnCl_4.5H_2O$ salts were used as precursors. At first, ethylene glycol and citric acid were dissolved as a 4:1 ratio at 70°C, and then 0.2 M $Ba(CH_3COO)_2$ and $SnCl_4.5H_2O$ were added to this solution. The solution was stirred until a transparent mixture was obtained. The final solution was divided into two equal amounts. For the FSP method, the resulted solution was fed to flame spray pyrolysis equipment (Tethis Nps10) using the glass syringe to obtain BSO particles. To investigate the changing in phase structure of BSO particles, all of the powders were annealed at different temperatures as 600°C, 800°C, 1000°C, and 1200°C, respectively. In order to facilitate the interpretation of the results, $BaSnO_3$ particles synthesized by FSP were encoded as BSO_FSP.

2.4 Preparation of BSO_FSP based thin-film sensors

In the production of the sensing slides, ethyl cellulose (EC) was chosen as support material because of the high diffusibility of the solvent vapors. In this work, the sensing material was prepared by mixing 100 mg of EC and 0.25 mg of BSO_FSP in 2.5 mL of THF. All of the constituents were mixed under magnetic stirring. The prepared polymeric mixture was spread onto polyester support (Mylar TM type) by knife coating technique. Tencor Alpha Step 500 Prophylometer was used to measure thicknesses of the coated thin films. The average thickness of the films was found to be 7.25 ± 0.13 μm (n = 5).

2.5 Solvent vapors performance tests

The solvent vapor performance tests of the BSO_FSP nanoparticles were performed after exposure to various solvent vapors like ethanol (EtOH), acetone, and ammonia (NH_3) of the same test material in a closed desiccator. This group of tests was named “solvent vapors tests”. We exposed the sensor slides to the different concentrations of solvent vapors in a closed desiccator with an internal volume of 5 L by

placing 20 mL of solvent (contained in the 50 mL beaker). The vapors were obtained by evaporation of different solvents at room temperature. The mean laboratory temperature was 20°C (± 0.6°C) throughout the experiments. Concentrations of the solvent vapors were calculated using their partial vapor pressure at 20°C (EtOH: 5.95 kPa, acetone: 25.00 kPa, and NH_3 (25% v/v): 40.32 kPa). The partial pressures were also converted to per million part (ppm) for all of the solvent vapors were found to be 2.24, 11.90, and 5.60 (mg/20 ml) for the EtOH, acetone, and NH_3, respectively. Utilization of the BSO_ FSP crystals in ethyl cellulose in the form of thin films resulted in many advantages such as enhanced sensitivity and improvement in all optical gas sensing dynamics. Sensing characteristics of the offered composites were tested after exposure to vapors of EtOH, acetone, and NH_3, respectively.

3. Results And Discussion

3.1 Phase analysis (XRD)

The structural changes of the particles produced by the FSP method at different calcination temperatures were examined by XRD and the related patterns of the BSO particles were shown in Fig. 2. When the phase structure of the material was examined after the production, an amorphous structure was observed. At temperatures of 600 and 800 °C, a partially crystalline state began to form, but no full crystalline structure was formed. At temperatures of 1000 and 1200 °C, the material was crystalline, but at 1000 °C, besides the $BaSnO_3$ phase with cubic perovskite structure, the SnO_2 phase was also determined. At 1200 °C the material was found to have a completely $BaSnO_3$ structure. All the peaks agree with the reported JCPDS data (Card No. 15-780). These results are consistent with the studies in the literature [18,22,23].

The structural and lattice parameters of the BSO material were calculated with the Rietveld refinement using the Maud 2.71V software and detailed results are given in Table 1. The lattice parameters of the structure were compared with the JCPDS file (No. 15-0780) [24] for $BaSnO_3$ and very close values were observed. Based on the Rietveld analysis the structural parameters of $BaSnO_3$ were found to be a cubic perovskite structure with space group #221 (Pm3m) and lattice parameter 4.109A˚. Also, the crystalline size for the major (110) reflection of the BSO sample calcined at 1200 ^oC was determined to be 79.7 nm.

3.2 Elemental analysis (XPS)

The sample annealed at 1200 °C was analyzed by XPS for identification of the surface's chemical states and elements whose binding energies (BE) and weight concentration (wt%) were listed in Table 2. The binding energies of 777.75 eV, 485.23 eV, 529.32 eV, and 284.93 eV are corresponding to Ba3d, Sn3d, O1s, and C1s, respectively which is shown in Fig. 3a. The C1s peak at 284.93 eV is owing to the carbon contamination which comes from carbon tape used for binding powders to the holder for analyses [25,26]. Ba3d and Sn3d are composed of two doublet peaks which are termed as $d_{3/2}$ and $d_{5/2}$ while O1s and C1s are present in single and/or deconvoluted peaks. $Ba3d_{3/2}$ and $Ba3d_{5/2}$ are the doublet peaks of Ba3d and peak positions are 792.58 eV and 777.28 eV, respectively which are depicted in Fig. 3b. The

difference between these peaks is 15.30 eV which is corresponding with the Ba^{2+} state [25,27]. Sn3d consists of doublet peaks of $Sn3d_{5/2}$ (485.08 eV) and $Sn3d_{3/2}$ (493.48 eV) which are shown in Fig. 3c and peak differences between these are 8.4 eV which is related to Sn^{4+} state [25,27,28]. The deconvoluted O1s core level spectra are shown in Fig. 3d. The peak of 529.32 eV is related to lattice oxygen while the peak of 532.05 eV is related to surface hydroxyl groups [29–31]. XPS survey and core level spectra confirm that Ba, Sn, and O are the valence states of 2+, 4+, and 2- that forms cubic perovskite $BaSnO_3$ and inhibit the presence of any other metal-oxygen composites [32].

3.3 FTIR measurements

To get information on the evolution of the functional groups and confirm the composition during the crystallization of the synthesized powders, the annealed powders at different temperatures from each synthesis method were characterized using FTIR spectroscopy. Fig. 4 shows FTIR spectra of BSO_FSP particles as before annealed and calcined at from 600 to 1200 °C. As seen from this graph, the broad bands at approximately 3400 cm^{-1} and 1600 cm^{-1} can be attributed to hydroxide (H–OH) vibrational and flexing mode, respectively. The band occurs approximately at 1420-1430 cm^{-1} is due to the vibration of the residual organic C–H groups. On the other hand, the bands at 611 and 623 cm^{-1} correspond to the Sn-O. All the bands of these spectra agree with the literature [23,33].

3.4 Particle morphology and size distribution measurements

SEM images and particle size measurements were performed to look into the morphology, size distribution of the BSO_FSP particles calcinated at 1200 °C, and the results were shown in Fig. 5. The annealed particles at 1200 °C with a dimension of between 400–1000 nm show a polyhedral shape morphology and the average size of the powders is calculated as approximately 700 nm. According to the obtained results, while the temperature is increasing to 1200 °C, the mean grain size of BSO_FSP powders grows from 70 nm to 980 nm and the size distribution of particles becomes wider. Because of the agglomeration, the powders obtained at 1200 °C contain relatively large grains with a size nearly to 1 μm.

3.5 Optical measurements

The reflectance spectra (See Fig. 6) measurements were performed by using UV-vis DRS to calculate the optical band gap of BSO_FSP at 1200°C with the following equation (See Eq. 1) [34]:

$$\alpha h\nu = A(h\nu - E_g)^n \qquad (1)$$

where α is absorption coefficient, h is Planck's constant, ν is the frequency of incident photons, A is the energy-independent constant, E_g is bandgap and n is the index determining the type of transitions and could be values of 2, 3, 1/2, and 3/2 for indirect allowed, indirect forbidden, direct allowed, and indirect forbidden transition, respectively [35]. Kubelka-Munk theory is commonly used to analyze the optical

band gap for materials that weakly absorb incident photons and function was applied to convert reflectance values to absorbance and determine optical bandgap [36]. The optical bandgap of the sample annealed at 1200 °C was determined with the help of the following Kubelka-Munk equation (See Eq. 2) [34]:

$$F(R) = \frac{(1-R)^2}{2R} \qquad (2)$$

where *F(R)* is the Kubelka-Munk function which is related with *α* as *α=F(R)/d (d is the thickness)*, and *R* is the reflectance. The results show that BSO_FSP annealed at 1200 °C has a 3.14 eV optical band gap and it is coherent with the literature [18,25,34].

The photoluminescence spectra that include the optical transitions of $BaSnO_3$ were shown in Fig. 7. The emission and excitation spectrum were measured at room temperature. When excited at 375 nm, the particles yielded sharp emission bands centered at 444, 485, 505, and 560 nm. The broad line at 444 is attributed to the transition of $^3P^0_0 - {}^3D_1$ of barium. The medium intense emission peak at 485 nm is due to the transitions of $^3P^0_1 - {}^1D_2$ of tin. The peak observed at 505 nm is referred to as the transitions of $^3P^2_0 - {}^3D_3$ of barium. The strong line at 560 nm is attributed to the transitions $^3P^0_0 - {}^3D_1$ of barium. Also, the crystals have strong emission band maxima at 944 nm in the near-infrared (NIR) region. A broad and strong near-infrared luminescence centered at 944 nm is attributed to the $BaSnO_3$ structure [37].

3.6 Optical gas sensing and decay time measurements

As can be seen in the former studies [7–12], the polyhedral shape structure encourages us to think that the large specific surface area of $BaSnO_3$ crystals improves gas sensing performance. Herein, we investigated the gas sensing properties of the BSO_FSP when exposing to the different solvent vapors. When excited at 375 nm, the split emission peaks appeared at 500 and 560 nm in the thin film form, respectively. The exposure time of the solvent vapors to BSO_FSP thin films was 60 min. at laboratory conditions. When the prepared thin films were exposed to the vapors of ethanol (EtOH), acetone, and ammonia (NH_3), both of the excitation and emission spectra of the BSO_FSP exhibited significant signal drop (See Fig. 8). As seen in Fig.8, the sensing materials exhibits sensitivities to the vapors of NH_3 ($I-I_0/I_0$ = 0.835), acetone ($I-I_0/I_0$ = 0.672) and EtOH ($I-I_0/I_0$ = 0.521), respectively. The increase in the surface area may have resulted in the enhancement of the interaction between the oxygen in the lattice structure of $BaSnO_3$ and the vapors of three different solvents.

However, in this study, the microsecond time scale decay time measurements of the BSO_FSP powder embedded in EC thin films when exposed to EtOH; acetone, and NH_3 were also investigated (see Fig. 9). The lifetime measurements also give us valuable information about the mechanism of interaction between the BSO_FSP powders and various solvent vapors. The decay curves of all BSO_FSP based thin films were well fitted by mono-exponential decay function when excited at 375 nm. Table 3 reveals the variation of the decay times in different vapors, EtOH, acetone, and NH_3. As seen from Table 3, the decay

time values of BSO_FSP powder in the EC matrix decreased from 11.11 µs to 11.03 µs, 10.62 µs, and 10.29 µs levels upon exposure to the vapors of EtOH, acetone, and NH_3, respectively. The surface adsorbed oxygen species and the enhancement in surface area play a very important role in the gas sensing process [38]. However, the similar decrease in decay time values as in intensity based measurements can be attributed to the interaction between oxygen in the lattice structure of $BaSnO_3$ and vapors of three different solvents.

4. Conclusion

$BaSnO_3$ particles, which were not previously produced by FSP, were successfully synthesized and the cubic phase structure was obtained at 1200 °C. As a result of the elemental analysis, no element was observed except the elements existing in the structure, and the structure was produced in the requested stoichiometric ratio. After morphological investigations, it was observed that the particles were polyhedral and the particle size was submicron. When the optical properties of the $BaSnO_3$ structure were examined, it was found to be a semiconductor material. $BaSnO_3$ particles exhibited maximum emission bands at 444, 485, 505 and 560 nm in the visible area, and also, a strong peak centered at 944 nm in the near-infrared region (NIR) under excitation at 375 nm.The intensity- and decay time- based gas sensitivities, which are one of the characteristics of perovskite $BaSnO_3$ structure, were studied optically and it was found to respond well to ethanol, acetone, and ammonia gas vapors. In the light of this information, it was determined that the synthesized material can be used in optoelectronic and gas sensor applications.

Declarations

Acknowledgment

Synthesis and characterization measurements performed at Dokuz Eylul University, Center for Fabrication and Applications of Electronic Materials.

References

1. M. G. Smitha and M. V Murugendrappa, Journal of Materials Science: Materials in Electronics **30**, 10776 (2019).
2. W. Zhang, J. Tang, and J. Ye, Journal of Materials Research **22**, 1859 (2007).
3. S. Upadhyay, O. Parkash, and D. Kumar, Journal of Electroceramics **18**, 45 (2007).
4. C. Shan, T. Huang, J. Zhang, M. Han, Y. Li, Z. Hu, and J. Chu, The Journal of Physical Chemistry C **118**, 6994 (2014).
5. B. Ostrick, M. Fleischer, U. Lampe, and H. Meixner, Sensors and Actuators B: Chemical **44**, 601 (1997).
6. K. F. Moura, L. Chantelle, D. Rosendo, E. Longo, and I. M. G. dos Santos, Materials Research **20**, 317 (2017).
7. I. A. Alagdal and A. R. West, Journal of Materials Chemistry C **4**, 4770 (2016).

8. L. M. Cavanagh, P. Smith, and R. Binions, Journal of The Electrochemical Society **159**, J67 (2011).
9. U. Lampe, J. Gerblinger, and H. Meixner, Sensors and Actuators B: Chemical **25**, 657 (1995).
10. A. Marikutsa, M. Rumyantseva, A. Baranchikov, and A. Gaskov, Materials **8**, 6437 (2015).
11. B. B. N. Anchal, P. Singh, and R. Pyare, Materials Today: Proceedings **18**, 1310 (2019).
12. S. Upadhyay and P. Kavitha, Materials Letters **61**, 1912 (2007).
13. J. Cerdà, J. Arbiol, G. Dezanneau, R. Dıaz, and J. R. Morante, Sensors and Actuators B: Chemical **84**, 21 (2002).
14. K. P. Ko, S. M. Choi, Y. C. Kim, J. W. Lee, S. H. Moon, C. Park, and S. I. Yoo, Physica C: Superconductivity and Its Applications **471**, 940 (2011).
15. É. Bévillon, A. Chesnaud, Y. Wang, G. Dezanneau, and G. Geneste, Journal of Physics: Condensed Matter **20**, 145217 (2008).
16. S. Moshtaghi, S. Zinatloo-Ajabshir, and M. Salavati-Niasari, Journal of Materials Science: Materials in Electronics **27**, 425 (2016).
17. J. Cerda, J. Arbiol, R. Diaz, G. Dezanneau, and J. R. Morante, Materials Letters **56**, 131 (2002).
18. K. Habeeba, T. E. Manjulavalli, D. V. E. GnanaKumari, and V. Karthikadevi, Materials Research Express **6**, 94004 (2019).
19. A. S. Deepa, S. Vidya, P. C. Manu, S. Solomon, A. John, and J. K. Thomas, Journal of Alloys and Compounds **509**, 1830 (2011).
20. J. John, V. P. M. Pillai, A. R. Thomas, R. Philip, J. Joseph, S. Muthunatesan, V. Ragavendran, and R. Prabhu, in *IOP Conference Series: Materials Science and Engineering* (IOP Publishing, 2017), p. 12007.
21. C. P. Udawatte, M. Kakihana, and M. Yoshimura, Solid State Ionics **108**, 23 (1998).
22. A. Sahmi, R. Laib, S. Omeiri, K. Bensadok, and M. Trari, Journal of Photochemistry and Photobiology A: Chemistry **364**, 443 (2018).
23. Y. H. O. Muñoz, M. Ponce, and J. E. R. Páez, Powder Technology **279**, 86 (2015).
24. H. D. Megaw, Proceedings of the Physical Society **58**, 133 (1946).
25. J. John, S. R. Chalana, R. Prabhu, and V. P. Mahadevan Pillai, Applied Physics A: Materials Science and Processing **125**, 1 (2019).
26. J. F. Moulder, W. F. Stickle, P. E. Sobol, and K. D. Bomben, Perkin-Elmer Corp., Eden Prairie, MN (1992).
27. P. Singh, B. J. Brandenburg, C. P. Sebastian, P. Singh, S. Singh, D. Kumar, and O. Parkash, Japanese Journal of Applied Physics **47**, 3540 (2008).
28. P. Nithyadharseni, M. V. Reddy, K. I. Ozoemena, F. I. Ezema, R. G. Balakrishna, and B. V. R. Chowdari, Journal of the Electrochemical Society **163**, A540 (2016).
29. M. Kim, B. Lee, H. Ju, J. Y. Kim, J. Kim, and S. W. Lee, Advanced Materials **31**, 1903316 (2019).
30. S. Yildirim, S. A. Akalin, S. Oguzlar, M. Z. Ongun, C. Ozer, and M. Erol, Journal of Materials Science: Materials in Electronics **30**, 13749 (2019).

31. J. Socratous, K. K. Banger, Y. Vaynzof, A. Sadhanala, A. D. Brown, A. Sepe, U. Steiner, and H. Sirringhaus, Advanced Functional Materials **25**, 1873 (2015).
32. A. Roy, P. P. Das, P. Selvaraj, S. Sundaram, and P. S. Devi, ACS Sustainable Chemistry and Engineering **6**, 3299 (2018).
33. S. V Manorama and V. J. Rao, Journal of Materials Science: Materials in Electronics **12**, 137 (2001).
34. R. Köferstein and F. Yakuphanoglu, Journal of Alloys and Compounds **506**, 678 (2010).
35. Z. Yang, H. Peng, W. Wang, and T. Liu, Journal of Applied Polymer Science **116**, 2658 (2010).
36. B. Hadjarab, A. Bouguelia, and M. Trari, Journal of Physics D: Applied Physics **40**, 5833 (2007).
37. H. Mizoguchi, P. M. Woodward, C.-H. Park, and D. A. Keszler, Journal of the American Chemical Society **126**, 9796 (2004).
38. X. Chu, Z. Gan, L. Bai, Y. Dong, and M. N. Rumyantseva, Materials Science and Engineering: B **259**, 114606 (2020).

Tables

Table 1. Detailed crystallographic parameters of BSO_FSP at 1200 ^{o}C

Samples	2θ of crystal Plane (110)	Lattice parameters (Å)	Unit Cell Volume $(Å)^3$	Average Crystallite Size (nm)	d-spacing (Å)
$BaSnO_3$ (JCPDS 15-780)	30.75	a=b=c= 4.109 β= 90	69.35	-	2.905
BSO_FSP at 1200 ^{o}C	30.76	a=b=c= 4.108 β= 90	69.32	79.7	2.905

Table 2. Binding Energy (BE) and atomic weight (%) values according to the XPS survey of BSO_FSP annealed at 1200°C

Sample Name	Name	Peak BE	Weight %
BSO_FSP at 1200°C	Ba3d	777.75	42.11
	Sn3d	485.23	31.18
	O1s	529.32	20.47
	C1s	284.93	6.24

Table 3. Phosphorescence decay time measurements of the BSO_FSP powder embedded in EC thin films exposed to different solvent vapors as EtOH; acetone and NH_3.

Sample	τ_0	Decay Time (µs)	Std. Dev. (µs)	Rel. (%)	τ_{avr}
BSO_FSP	τ_1	11.1108	0.16858	100	11.11
BSO_FSP + EtOH	τ_1	11.0349	0.15951	100	11.03
BSO_FSP + acetone	τ_1	10.6179	0.10234	100	10.62
BSO_FSP + NH_3	τ_1	10.2899	0.10037	100	10.29

Figures

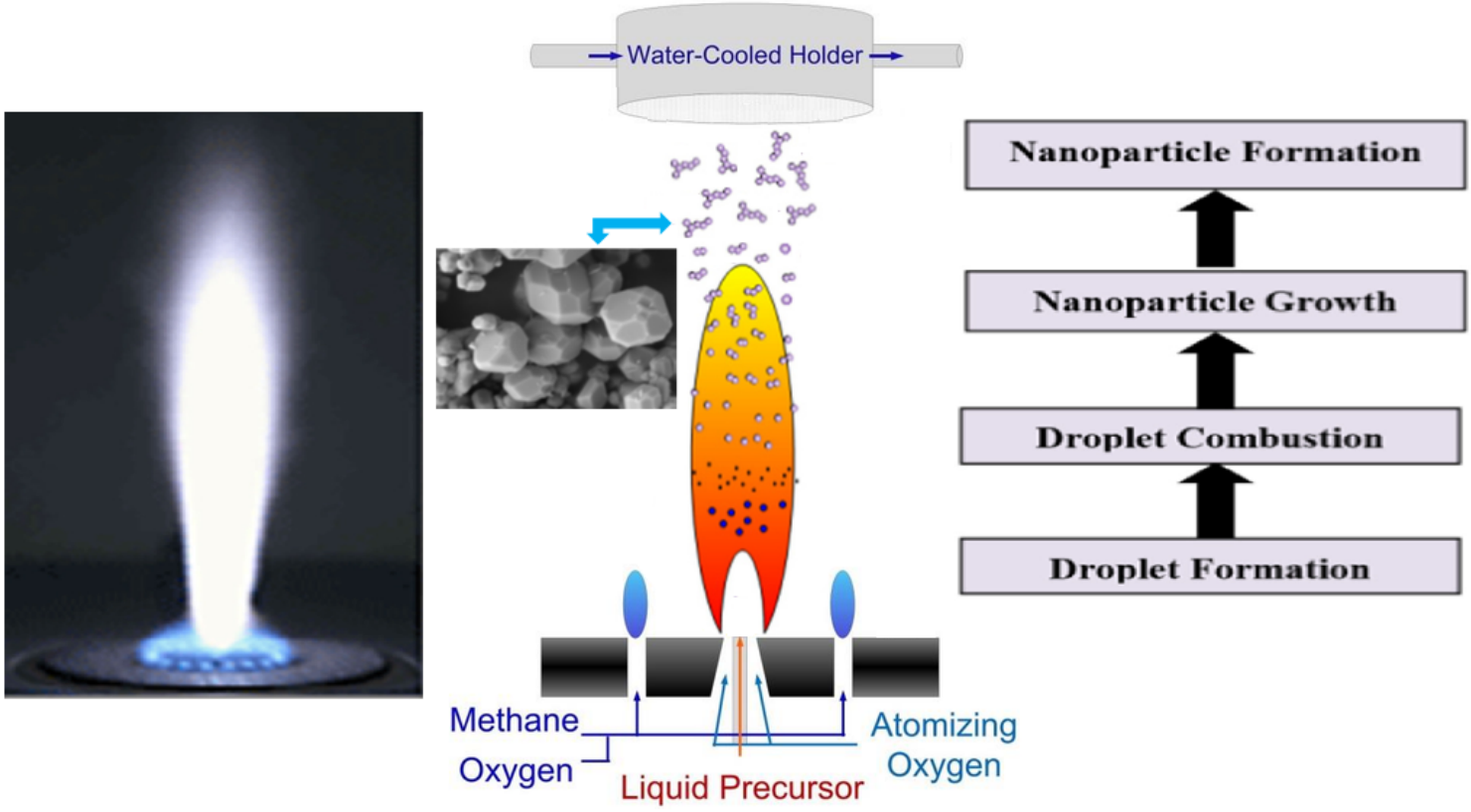

Figure 1

Flow chart of flame spray pyrolysis synthesis

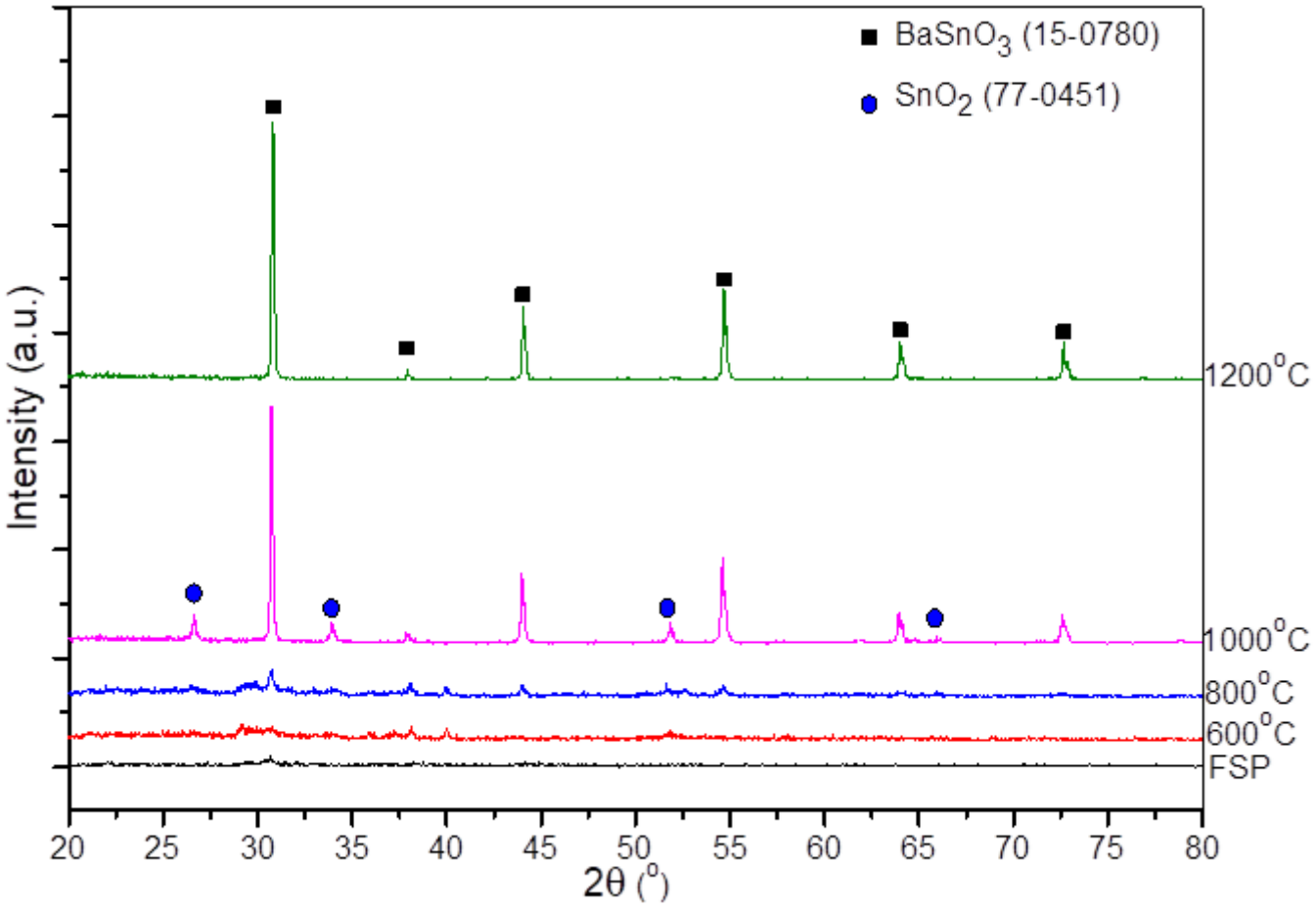

Figure 2

XRD patterns of BSO_FSP particles at different temperatures

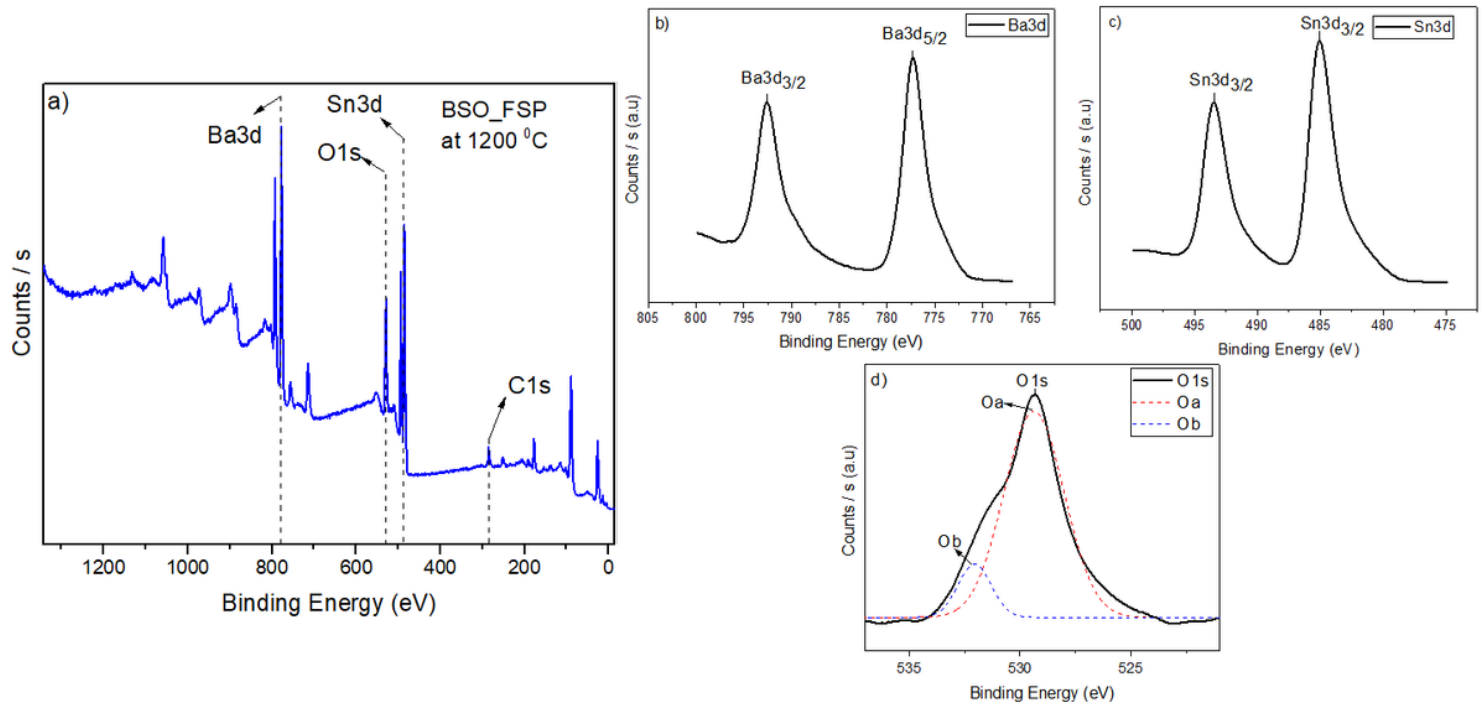

Figure 3

XPS survey spectra of (a) BSO_FSP annealed at 1200°C, core level spectra of (b) Ba3d, (c) Sn3d, and (d) O1s

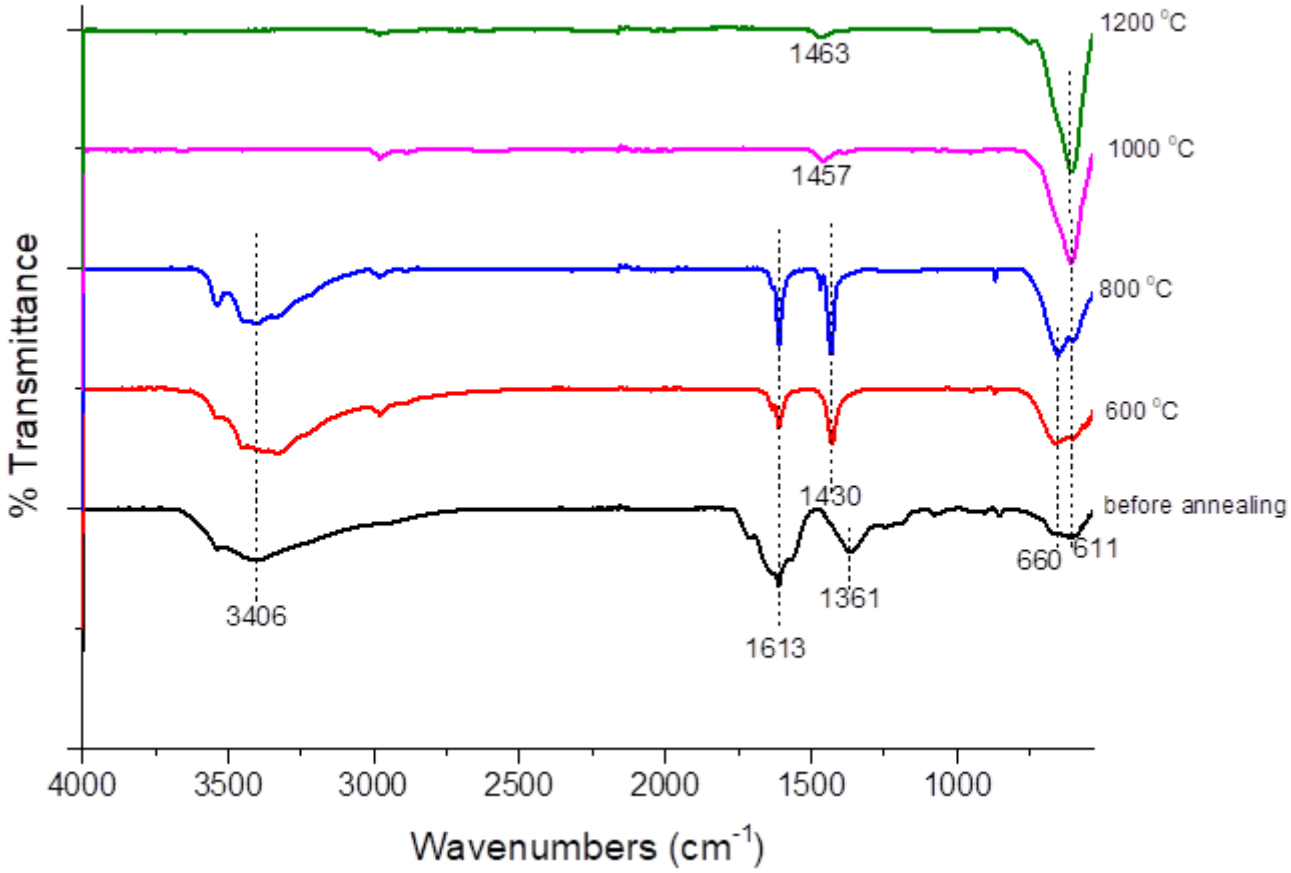

Figure 4

FTIR spectra of the BSO_FSP at different temperatures

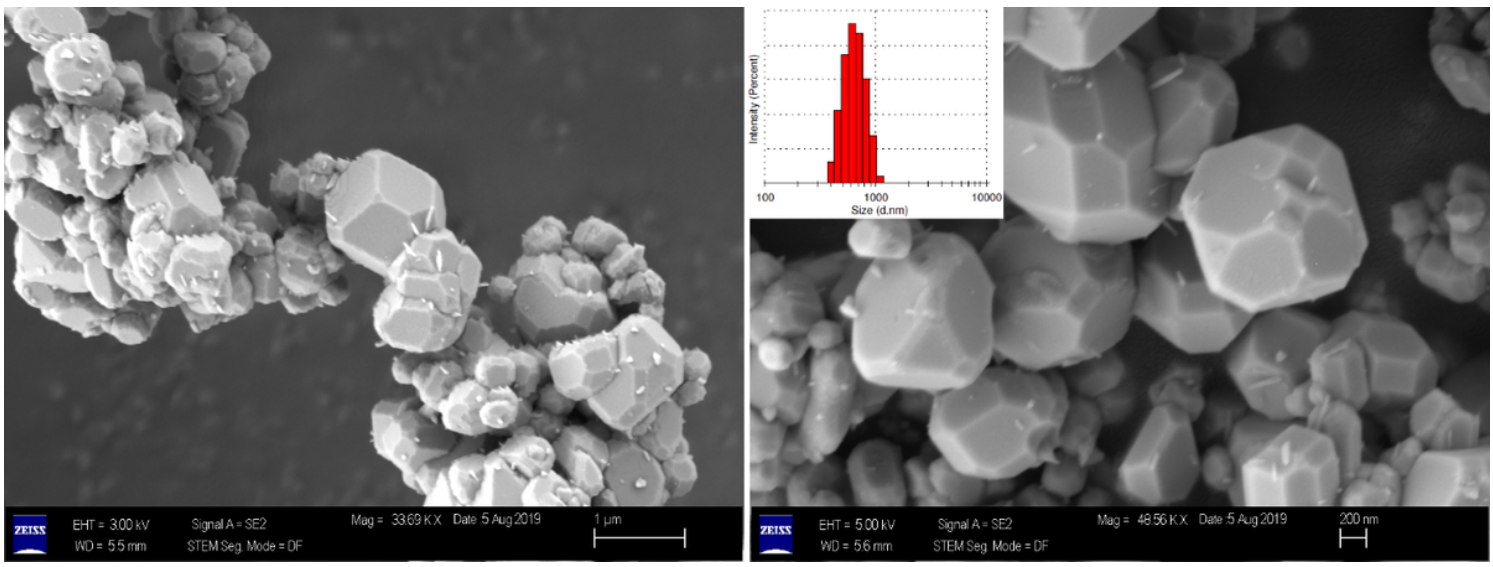

Figure 5

SEM images and particle size distribution of BSO_FSP powders at different magnifications

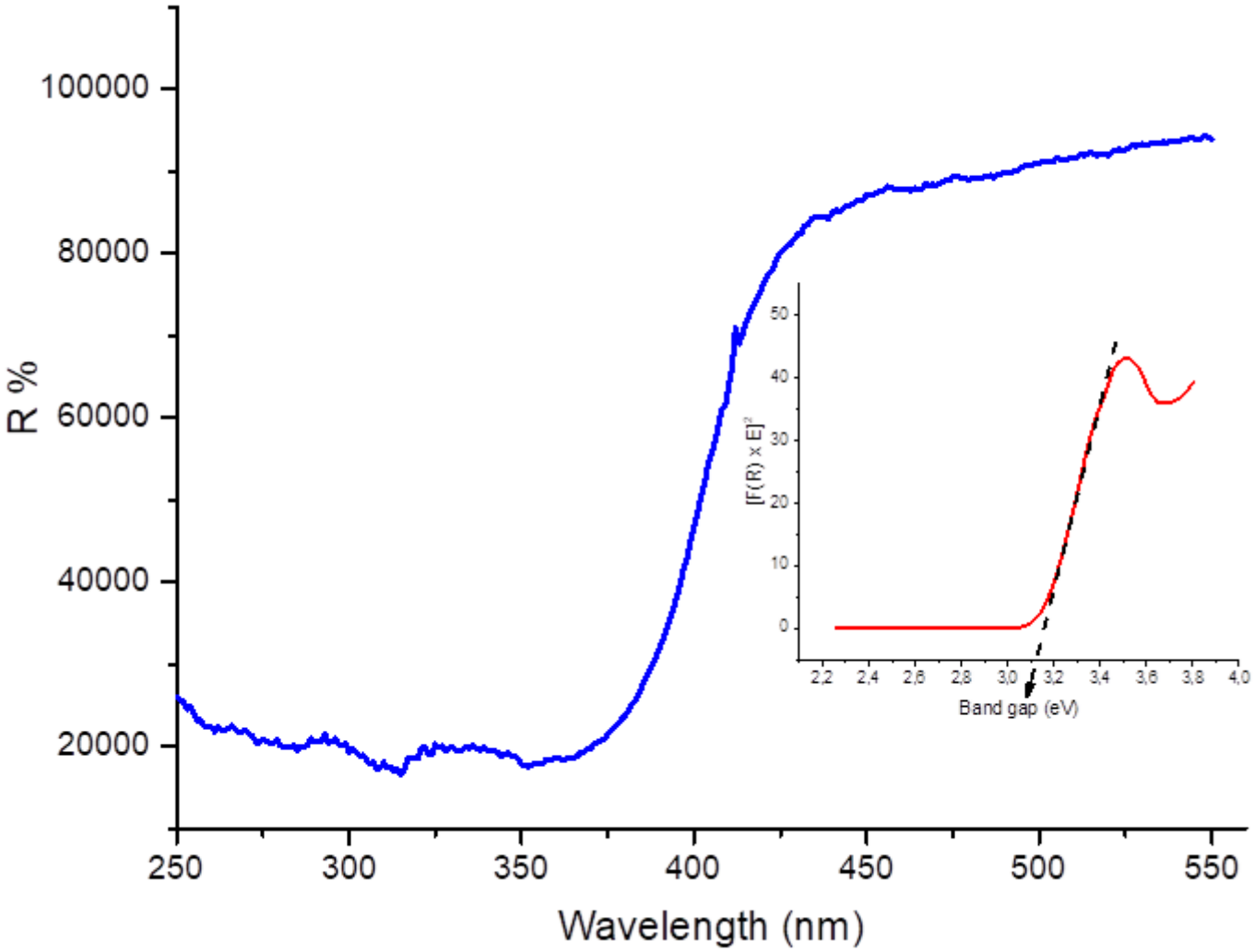

Figure 6

Reflectance spectra of BSO_FSP / Inset: The calculation of band gap value with the Kubelka-Munk method.

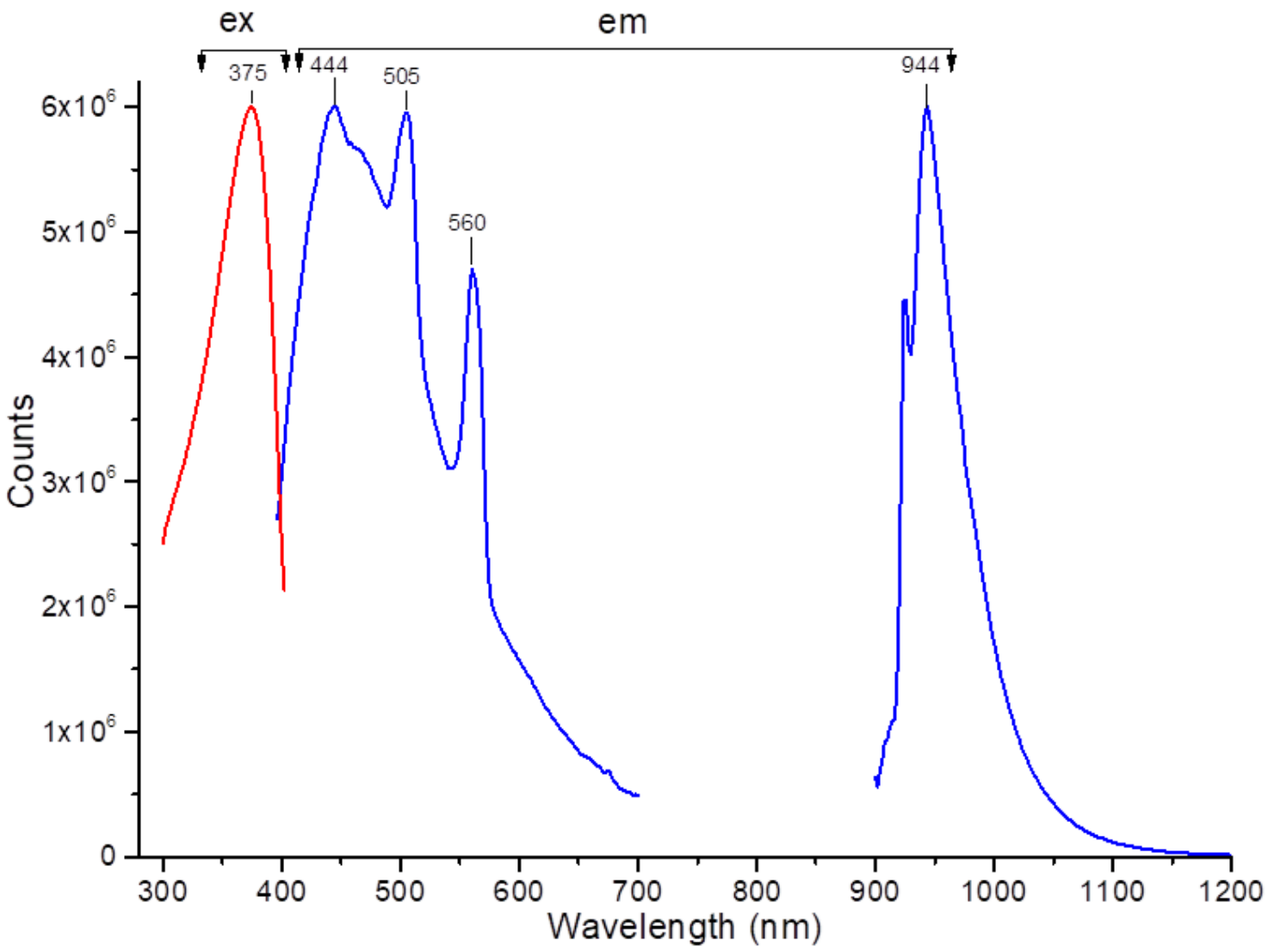

Figure 7

Excitation and emission spectra of BaSnO3 for the FSP method

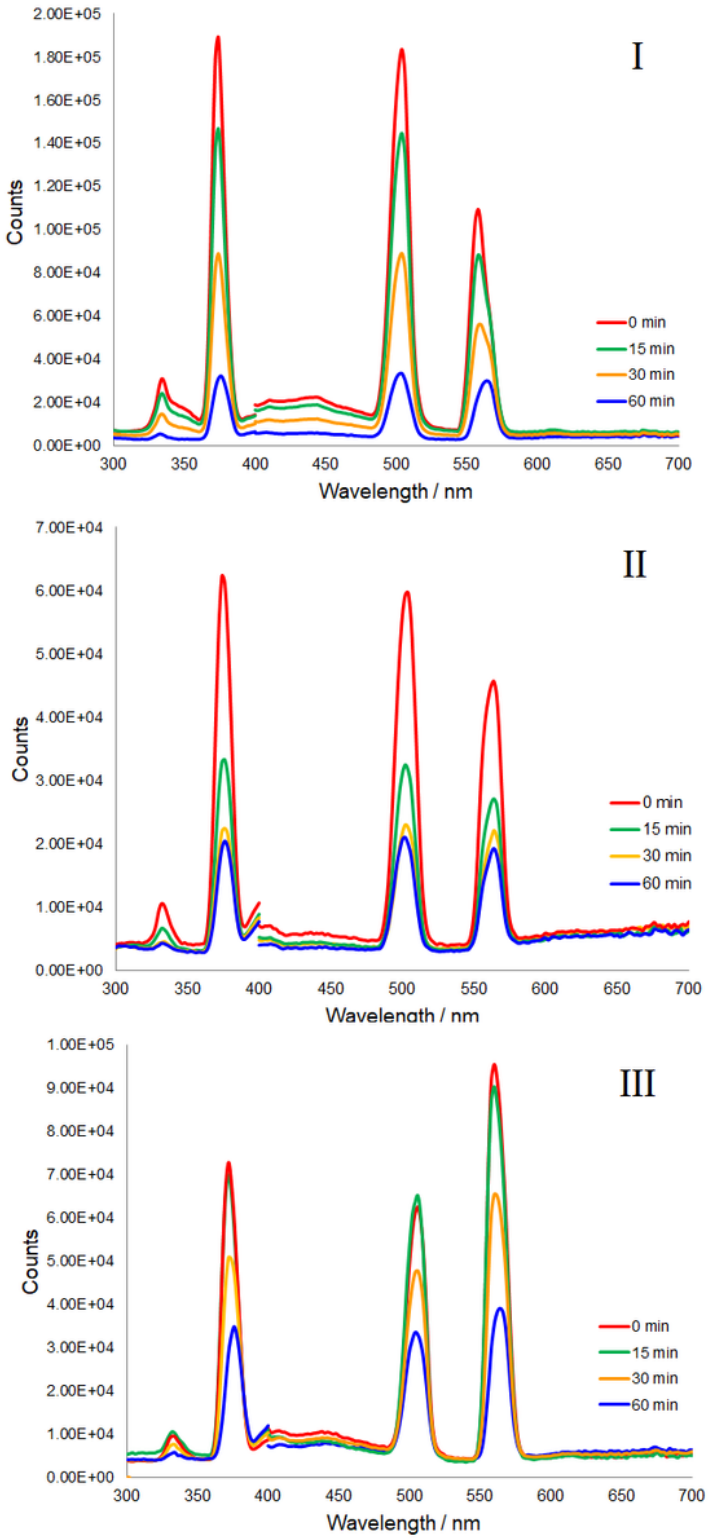

Figure 8

The intensity-based response of the BSO_FSP powder embedded in EC thin films exposed to solvent vapors as NH3, acetone and EtOH.

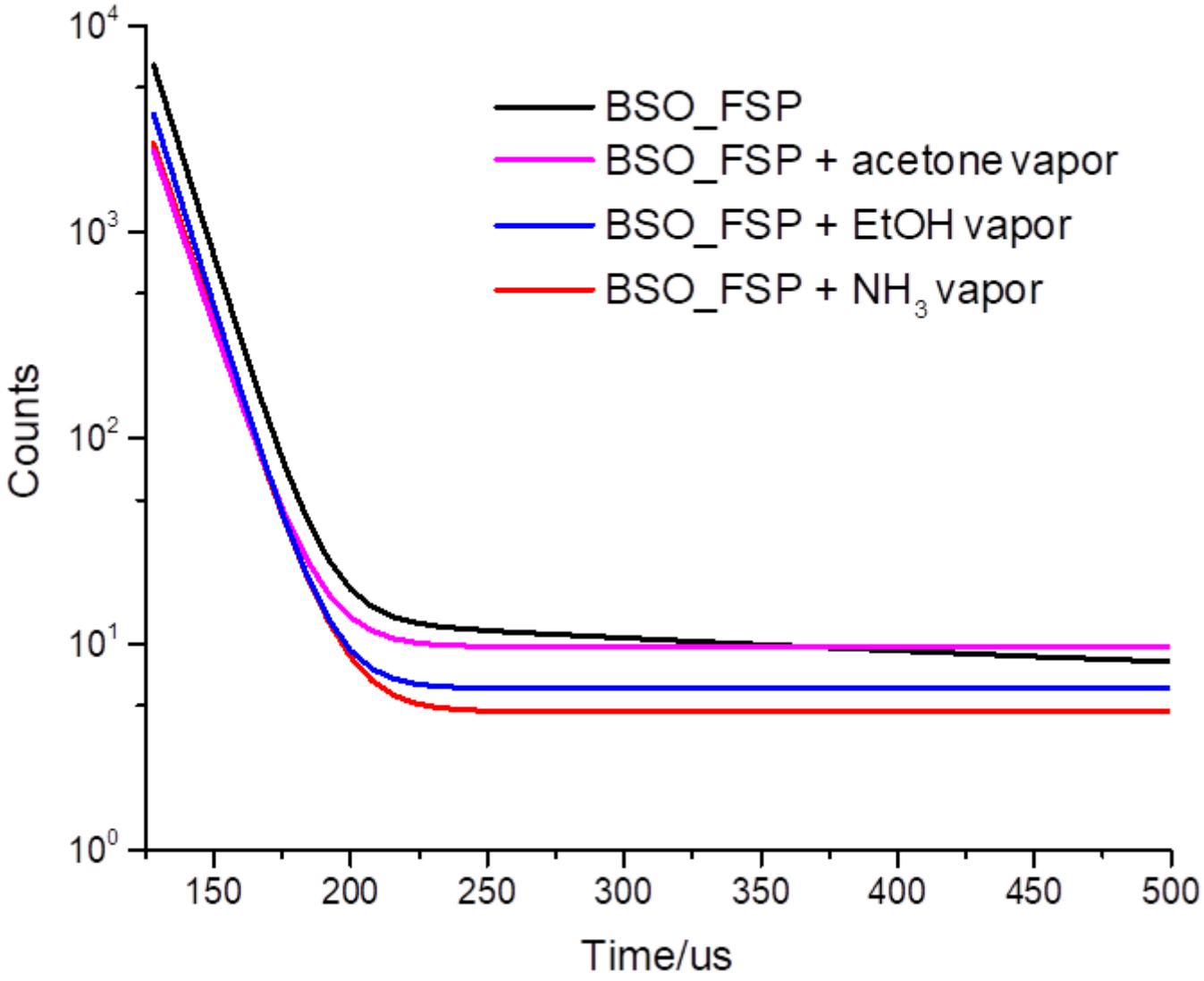

Figure 9

The fitted decay time spectra of the BSO_FSP powder embedded in EC thin films exposed to solvent vapors as NH3, acetone and EtOH.